





## Exploiting ionization dynamics in the nitrogen vacancy center for rapid, high-contrast spin, and charge state initialization

D. Wirtitsch <sup>1,2</sup> G. Wachter,<sup>1</sup> S. Reisenbauer <sup>1,3</sup> M. Gulka <sup>4,5</sup> V. Ivády,<sup>6,7,8</sup> F. Jelezko,<sup>9</sup>  
A. Gali <sup>10,11</sup> M. Nesladek,<sup>4,12</sup> and M. Trupke<sup>1,2,\*</sup>

<sup>1</sup>Vienna Center for Quantum Science and Technology, Department of Physics, University of Vienna, Boltzmannngasse 5, A-1090 Vienna, Austria

<sup>2</sup>Institute for Quantum Optics and Quantum Information (IQOQI) Vienna, Austrian Academy of Sciences, Boltzmannngasse 3, A-1090 Vienna, Austria

<sup>3</sup>AIT Austrian Institute of Technology GmbH, Giefinggasse 4, A-1210 Vienna, Austria

<sup>4</sup>Institute for Materials Research, University of Hasselt, Wetenschapspark 1, 3590 Diepenbeek, Belgium

<sup>5</sup>Institute of Organic Chemistry and Biochemistry, Academy of Sciences of the Czech Republic, Flemingovo náměstí 2, 166 10 Prague 6, Czech Republic

<sup>6</sup>Department of Physics of Complex Systems, ELTE Eötvös Loránd University, Egyetem tér 1-3, H-1053 Budapest, Hungary

<sup>7</sup>MTA-ELTE Lendület “Momentum” NewQubit Research Group, Pázmány Péter, Sétány 1/A, 1117 Budapest, Hungary

<sup>8</sup>Department of Physics, Chemistry and Biology, Linköping University, 581 83 Linköping, Sweden

<sup>9</sup>Institute of Quantum Optics, Ulm University, Ulm 89081, Germany

<sup>10</sup>Institute for Solid State Physics and Optics, Wigner Research Centre for Physics, P.O. Box 49, H-1525 Budapest, Hungary

<sup>11</sup>Department of Atomic Physics, Institute of Physics, Budapest University of Technology and Economics, Műegyetem rakpart 3, H-1111 Budapest, Hungary

<sup>12</sup>IMOMECE, Division IMEC, Wetenschapspark 1, 3590 Diepenbeek, Belgium



(Received 2 March 2021; accepted 21 November 2022; published 13 January 2023)

We propose and experimentally demonstrate a method to strongly increase the sensitivity of spin measurements on nitrogen vacancy (NV) centers in diamond, which can be readily implemented in existing quantum sensing experiments. While charge state transitions of this defect are generally considered a parasitic effect to be avoided, we show here that these can be used to significantly increase the NV center’s spin contrast, a key quantity for high-sensitivity magnetometry and high-fidelity state readout. The protocol consists of a two-step procedure, in which the charge state of the defect is first purified by a strong laser pulse, followed by weak illumination to obtain high spin polarization. We observe a relative improvement of the readout contrast by 17% and infer a reduction of the initialization error of more than 50%. The contrast enhancement is accompanied by a beneficial increase of the readout signal. For long sequence durations, typically encountered in high-resolution magnetometry, a measurement speedup by a factor of  $>1.5$  is extracted, and we find that the technique is beneficial for sequences of any duration. Additionally, our findings give detailed insight into the charge and spin polarization dynamics of the NV center and provide actionable insights for direct optical, spin-to-charge, and electrical readout of solid-state spin centers.

DOI: [10.1103/PhysRevResearch.5.013014](https://doi.org/10.1103/PhysRevResearch.5.013014)

### I. INTRODUCTION

Spin centers in crystals such as diamond and silicon carbide are prime candidates for the development of quantum sensors given their long quantum coherence lifetimes and strong optical transitions [1–13]. In diamond, the nitrogen vacancy (NV) center is particularly prominent due to its excellent room-temperature spin coherence, high brightness, and

large optical spin contrast. The defect, which consists of a substitutional nitrogen atom and an adjacent vacancy in the diamond lattice, displays multiple charge states [14], of which the negative state  $NV^-$  is commonly discussed due to its optically addressable spin-1 ground state. However, the charge state dynamics have gained increasing interest in recent years, spurred in part by the observation of spin-to-charge conversion [15]. This mechanism forms the basis of photoelectric detection of the NV center’s magnetic resonance (PDMR) and its coherent dynamics, down to the single-defect level [16–19]. Since this development removes the need for collection optics and single-photon detectors, it makes the NV center system more amenable to integrated technological applications, particularly in compact diamond quantum sensors [20–22].

The sensitivity of such a diamond sensor depends on the optical spin readout contrast and on the signal strength (i.e.,

\*Author to whom correspondence should be addressed: michael.trupke@univie.ac.at

Published by the American Physical Society under the terms of the Creative Commons Attribution 4.0 International license. Further distribution of this work must maintain attribution to the author(s) and the published article’s title, journal citation, and DOI.

the square root of the photon collection rate), motivating numerous efforts to improve each of these quantities [23]. Typical single-NV-center experiments obtain a readout contrast of about 30%.

Recently, a relative increase of about 10% was reported by using a multipulse spin initialization routine with short green laser pulses at a single power, applied in alteration with wait periods over a total duration of several microseconds [24]. However, the charge state dynamics of the center were not considered therein.

Charge state initialization is a key factor towards improving the readout contrast, since population in the neutral state ( $NV^0$ ) leads to undesirable background luminescence and reduced brightness. However, a major hindrance in charge state initialization lies in the unfavorable ionization dynamics that only allow unidirectional conversion from  $NV^-$  to  $NV^0$  via excitation with a wavelength longer than the zero-phonon line of  $NV^0$ . Unfortunately, no such mechanism has been shown for the transfer from  $NV^0$  to  $NV^-$ . The importance of charge state purity for increased measurement sensitivity was highlighted in another recent experiment, where the center's charge state was controlled in real time via fast electronic feedback [25]. Although this method achieved high-fidelity charge state initialization and an increase in the contrast by a factor of  $\sim 1.13$ , it required an initialization duration of several tens of microseconds and considerable hardware overhead.

Here, we predict and demonstrate a method to improve the readout contrast and brightness by enhanced charge and spin state initialization of the NV center. The method is readily suitable for existing experimental setups. We find that this sequence provides superior initialization for any measurement duration and we thereby improve the collected photon rates by 11% and the maximal readout contrast to  $>46\%$ . It requires only excitation using a single wavelength with different powers, and we demonstrate experimentally that most of the resulting improvement can be obtained using very short pulse sequences with a combined length of less than  $3\ \mu\text{s}$ , providing enhanced readout for any measurement sequence length. Furthermore, the principle is most likely applicable to a whole host of similar systems, such as the divacancy, the silicon vacancy, and NV centers in silicon carbide, as well as similar defects in other materials [9–11,13,26,27].

## II. MODEL: CHARGE STATE DYNAMICS TO IMPROVE SIGNAL AND CONTRAST

We develop an effective rate equation model which includes both the spin and the charge dynamics to reproduce the experimental time traces and the derived spin contrasts. A conceptual overview of the scheme is shown in Fig. 1(a). The model utilizes the decay rates  $\Gamma_{ji}$  and absorption cross sections  $\sigma_{ij}$ , with  $i$  and  $j$  corresponding to the involved levels. The free parameters in the model are the excitation cross sections, all decay rates, and overall scaling factors for the excitation rates of the two lasers. The resulting parameters are found by a least-squares minimization procedure described in detail in Appendixes A, B, and G. Our model consists of five levels in the negatively charged center (two ground states, two excited states, and one singlet level) and two levels in the neutral state. We do not include any metastable levels in

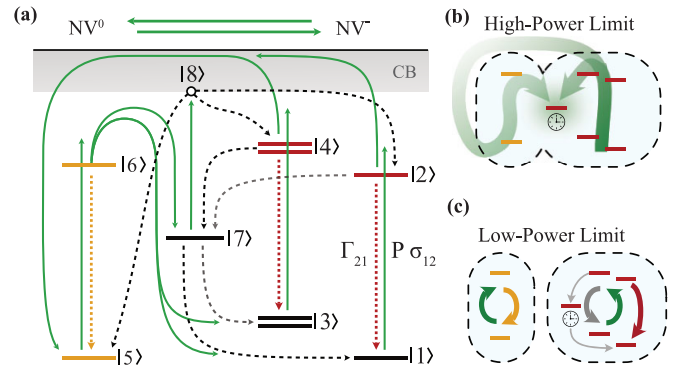


FIG. 1. Model overview. (a) Level diagram (levels 1–8) used for model predictions including a charge capture channel into the metastable state (level 7). Green arrows denoted by a  $\sigma$  indicate a laser-driven transition, while system-internal decay processes are indicated by dashed arrows and denoted by a  $\Gamma$ . CB, conduction band. (b) Sketch of population distribution within the NV center under high-power illumination. At strong saturation, a significant portion of the NV center population will be shelved in the longest-lived state, i.e., the  $NV^-$  metastable state. (c) Under low-power illumination, the population within the  $NV^-$  manifold will be spin polarized by the intersystem crossing dynamics, while the quadratic power dependence suppresses two-photon charge state mixing processes.

the neutral charge state. It is known that the  $NV^0$  charge state possesses a metastable manifold which has been observed by electron spin resonance [28]. From this manifold a one-photon charge state conversion is energetically possible [29]. Previous observations, however, indicate that this process does not play a significant role in the charge state dynamics of the system [30–32]. Finally, a weakly bound state is included as described below.

A two-photon process via level 6 effects the  $NV^0$  to  $NV^-$  transition [30–32]. *Ab initio* considerations indicate that the conversion from  $NV^0$  to  $NV^-$  occurs from the optically excited  $NV^0$  state (level 6) both directly to levels 1 and 3 and via the metastable singlet state (level 7) (see Appendix A). This state exhibits a lifetime which is more than an order of magnitude longer than all optically excited states and has a small excitation cross section that allows the population to be shelved during illumination [1,17]. This conversion pathway highlights the close relationship between the spin, the charge state, and the shelving dynamics which has eluded a detailed description so far [18].

This optical pathway connects the charge state dynamics with a shelving process in the long-lived singlet state. In the (optical) high-power limit, this mechanism enables efficient charge state initialization via  $NV^-$  to  $NV^0$  transfer and subsequent electron recapture [Fig. 1(b)]. The model indicates that the negative charge state population can thereby be increased from  $\sim 80\%$  at low power to over 92% (see Appendix B). However, increased shelving under high-power illumination, i.e., far beyond saturation of the optical transition, would lead to continuously decreased luminescence with higher laser powers, while it has been shown that the NV center exhibits almost power-independent luminescence in this regime [33,34]. This behavior is accounted for in the model by allowing excitation out of the singlet state via

single-photon absorption to a higher-lying state [level 8 in Fig. 1(a)] [33,35]. Including this state, the luminescence is expected to slightly decrease past the saturation point while remaining almost constant at higher laser powers, consistent with the anomalous saturation behavior observed previously [33,34,36]. Nonetheless, high-power illumination overall provides a method to significantly improve the charge state purity.

After shelving, the  $NV^- m_s = 0$  occupation will be limited to only 81% of the total population, by a combination of the branching ratio of the decays from the metastable state and excitation out of the metastable state, according to our model (see Appendix B). Using high-power initialization, we therefore sacrifice spin state purity to improve the charge state ratio. However, the  $m_s = 0$  population can now be increased by using weak excitation: For sufficiently low laser power, charge state conversion becomes negligible as it is suppressed due to its quadratic dependence on the illumination intensity [37] [Fig. 1(c)]. The spin polarization is then constrained by the ratio of the spin mixing rates, with a limiting value of 98% in the  $m_s = 0$  state within the  $NV^-$  manifold, resulting in >90% of the total population residing in the  $m_s = 0$  state. In comparison, conventional initialization results in only ~77% of the total population residing in  $m_s = 0$  (see Appendix B). Thus, using sufficiently weak laser pulses, two-power initialization is able to improve both charge and spin state purity. However, it should be noted that in practice the achievable spin polarization will be a compromise between expediency and charge purity.

### III. EXPERIMENTAL RESULTS

For our measurements, we use a home-built optically detected magnetic resonance (ODMR) setup with two 520-nm, 80-mW laser diodes (Roithner LD-520-80MG). Two separate diodes are used here in order to guarantee that the readout pulses for different sequences are not affected by thermal changes, or any other memory effects in the diode which could be caused by different driving conditions. The diodes are driven by a directly transistor-transistor-logic-switchable (TTL-switchable) diode driver designed for spike-free switching (IC Haus HG1D). One laser diode is used for readout pulses only, while the second is used for the high- and low-intensity laser pulses. Their beams are combined on a polarizing beamsplitter and coupled into a single-mode, polarization-maintaining fiber with orthogonal polarizations. However, we note that two-power initialization can be achieved with a single laser diode.

As they have orthogonal linear polarizations, the two lasers couple differently to the NV center: The readout laser excites the optical transition 1.4 times more efficiently than the initialization laser. We use a readout laser power of  $P_R = 0.6$  mW, typical for NV center experiments, and initialization laser powers of <21 mW. Furthermore, in order to guarantee that our results are not altered by diode switching characteristics, we sample the incident beam and record time-resolved traces for both NV center fluorescence and laser power (see Appendix F).

The beam is focused on the sample by using an immersion-oil objective (Nikon CFI Plan Apo NCG 100X Oil) with a numerical aperture of 1.4 which is used for excitation as well

as for photon collection. For our optical system, the nominal intensity at the NV center is  $\sim 20$  mW/ $\mu\text{m}^2$  per milliwatt at the input of the microscope objective. Our model indicates that the resulting excitation rates are 35 and 25 MHz/mW for the readout and initialization laser, respectively.

$NV^0$  fluorescence is partially filtered out from the collected light by using a 650-nm long-pass filter. The luminescence is collected with two optical fibers (Thorlabs P5-SMF28) to identify single NV centers and detected by two avalanche photodiodes. Microwave pulses are produced with a signal generator (Analog Devices ADF4351), are amplified (Minicircuits ZHL-16W-43+), and reach the NV center via a wire spanned across the sample.

We operate at an external magnetic field close to 0 G, where the  $m_s = \pm 1$  states can be treated as degenerate, though we note that the scheme is equally applicable at larger fields, including those commonly used to polarize the nitrogen nuclear spin [38]. We further apply microwave pulses with a Rabi frequency of  $2\pi \times 13$  MHz, which is sufficient to efficiently drive all three transitions present due to hyperfine coupling between the nitrogen nucleus and the NV center's electronic spin [1].

#### A. Population shelving and contrast

In order to investigate the predicted reduction in luminescence due to shelving after high-power illumination, we use a  $P_R = 0.6$  mW readout laser pulse supplemented by  $P_D = 7$  mW pulses [Fig. 2(a)]. After a brief spike in the count rate, part of the luminescence is quenched by the high-power excitation. Switching off the strong laser pulse leads to a further, rapid decrease, after which the luminescence recovers on a timescale dependent on the metastable state's lifetime and the power  $P_R$ . No such behavior is observed when switching off the readout laser during the second strong pulse, corroborating the purported shelving due to intense illumination. Figure 2(b) shows the power dependence of the shelving up to  $P_D = 7$  mW. At even higher laser powers than measured here, our model predicts a minimum value of 0.35 for the fluorescence quench.

We compare the fluorescence traces obtained with and without application of a microwave  $\pi$  pulse [Fig. 2(c)], from which we directly calculate the respective readout contrasts. We define the contrast of an optically detected magnetic resonance (ODMR) signal as  $C = 1 - S_1/S_0$ , where  $S_1$  and  $S_0$  correspond to the total photon counts in the readout window from  $m_s = \pm 1$  and  $m_s = 0$ , respectively [39]. While a short integration time  $T_{\text{int}}$  near the start of the readout gives the highest contrast [Fig. 2(c)], a longer readout duration will increase the collected photon number. However, prolonged illumination leads to charge state conversion as well as spin depolarization, and thereby to a reduction of the contrast over time. We thus provide two distinct values: Maximal contrast is obtained from integrating over 50 ns near the start of the readout pulse. The contrast for a high signal-to-noise ratio (SNR) is instead obtained by integrating over a 280-ns window.

Figure 2(c) shows two spin state readout traces for two different initialization intensities, as well as the integration windows used to calculate the contrast values. The initialization powers used here are indicated by the blue area

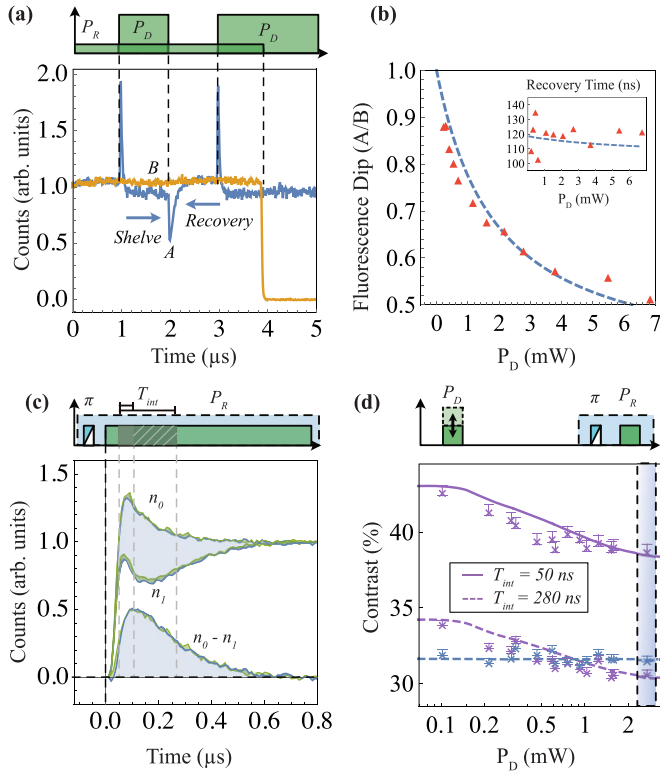


FIG. 2. High-power dynamics. (a) Photon collection during a  $P_R = 0.6$  mW readout pulse with (blue) and without (orange) additional  $P_D = 7$  mW pulses. The sudden decrease in fluorescence after switching off the strong pulse is indicative of shelving into a non-radiative state. (b) Depth of the fluorescence dip over  $P_D$  (red triangles) immediately after switching off the high-intensity laser. The dashed blue line is retrieved from our model, which reproduces the increased dip with laser power well. At higher laser powers, the model curve predicts a minimum value of 0.35 for the fluorescence quench. The inset shows the recovery time extracted from an exponential fit to the luminescence traces for different  $P_D$ . The dashed line is the recovery time obtained from the model. (c) Comparison of spin contrast luminescence traces for  $P_D = P_R = 0.6$  mW (blue) and  $P_D = 2$  mW with  $P_R = 0.6$  mW (green), where the latter corresponds to the highlighted data points in (d). The fluorescence counts collected with and without application of a microwave  $\pi$  pulse are denoted as  $n_1$  and  $n_0$ , while the lower graph corresponds to the signal difference between the two states. (d) We now apply the high-intensity laser pulse before the readout pulse and investigate the obtained contrast with increasing initialization power  $P_D$  using a pulse length of 3  $\mu$ s. Increasing  $P_D$  while keeping the readout power constant results in a decrease of the contrast (purple). We additionally show the reference contrast (blue) obtained from conventional initialization using a 0.6-mW initialization and readout pulse. We show both the maximal contrast (50-ns integration window) and the contrast for the highest signal-to-noise ratio (280 ns), from measurements (points) as well as numerical solutions from the model (lines). These integration windows are indicated by  $T_{\text{int}}$  in (c).

in Fig. 2(d). The blue trace shows our result for conventional initialization, while green lines are obtained from traces using 3 mW of initialization power. Here we obtain a slightly increased total luminescence signal, hinting at the increased charge state fidelity using high-power initialization. Furthermore, the reduction in readout contrast with laser

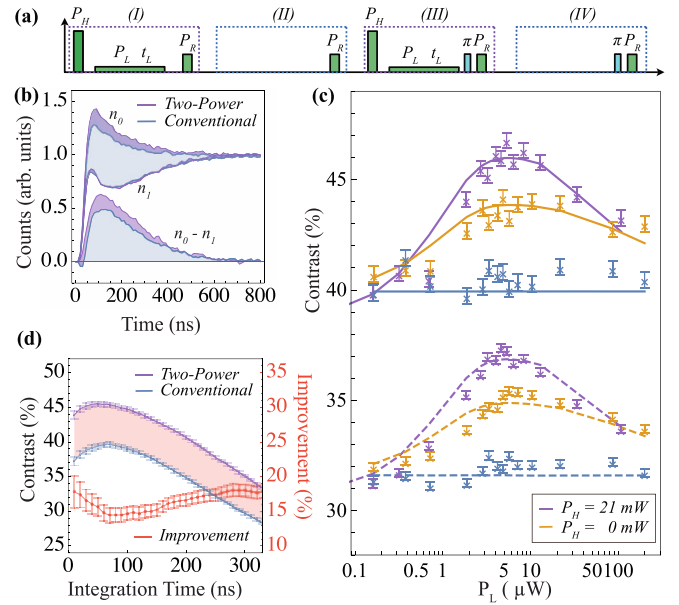


FIG. 3. Two-power enhancement. (a) Sequence used during measurements consisting of four steps (steps I–IV), for direct comparison of two-power (steps I and III) and conventional (steps II and IV) initialization, where the system is read out using the same laser power as for initialization. (b) Counts over time during a readout pulse for conventional initialization (blue) and with two-power initialization (purple). We observe a clear increase in the obtainable contrast at the start of the readout pulse, which reduces over time due to increased spin mixing. (c) Sweep of the power in the low-power pulse with a duration of 90  $\mu$ s after application of a  $P_H = 21$  mW charge state pulse (purple) and when omitting the latter (orange). Furthermore, we include the contrasts obtained from the conventional readout-pulse initialization for reference (blue). While crosses indicate data points, lines indicate numerical solutions from the model. We show both maximal (solid lines) and best-SNR (dashed lines) contrasts and for this duration obtain an optimal  $P_L \approx 6$   $\mu$ W. (d) Resulting contrast over increasing integration window duration for our two-power (purple) and conventional (blue) initialization. The red line shows the improvement evaluated for each integration time, which surpasses 17% for integration windows longer than 200 ns.

power is depicted in Fig. 2(d), where we vary the initialization power  $P_D$  while keeping the readout power fixed at  $P_R = 0.6$  mW.

## B. Two-power initialization

We now initialize our system using a two-power scheme. The system is initialized into the negative charge state via trapping in the metastable state by application of a high-intensity laser pulse with a power  $P_H = 21$  mW. We then apply a low-intensity pulse with power  $P_L = 6$   $\mu$ W and length  $t_L = 90$   $\mu$ s to polarize the spin state via the more favorable excited-state branching ratios within  $\text{NV}^-$ , followed by a readout pulse [see step I in Fig. 3(a)]. We additionally perform measurements with the conventional (single-pulse single-power) readout-pulse initialization method [see step II in Fig. 3(a)].

In order to quantify the effects of the charge state initialization pulse (with power  $P_H$ ) and the spin initialization pulse (power  $P_L$  and length  $t_L$ ), we first fix  $P_H = 21$  mW and

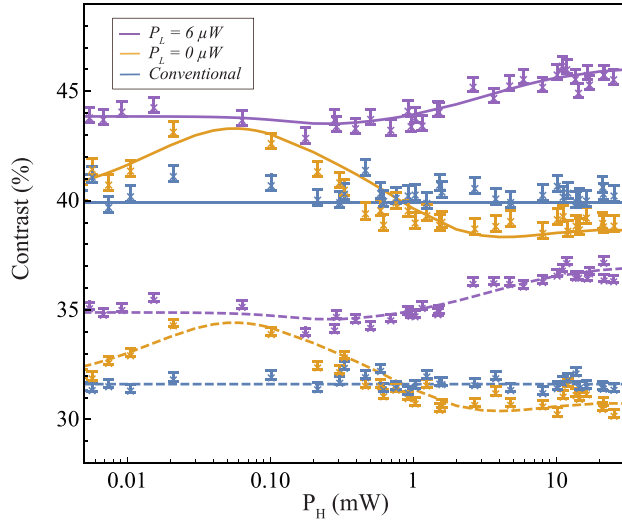


FIG. 4. Contribution of the charge initialization pulse. High-intensity laser power sweep for  $P_L = 6 \mu\text{W}$  (purple) and  $P_L = 0 \mu\text{W}$  (orange) for maximal contrast (solid lines) and best-SNR contrast (dashed lines). We additionally show our obtained contrast using conventional readout-pulse initialization (blue). Lines are obtained from solving the model, while crosses indicate data points.

$t_L = 90 \mu\text{s}$  while varying the power  $P_L$  [see Fig. 3(c)]. We observe a fairly wide optimum around  $P_L = 6 \mu\text{W}$  for which a maximal contrast around 46% can be reached using the two-power sequence, compared with  $\sim 43.5\%$  using only the low-power pulse.

Having chosen a power  $P_L$ , we aim to quantify the charge state initialization by varying the power of the high-intensity laser, as depicted in Fig. 4. We perform these measurements once for  $P_L = 6 \mu\text{W}$  (purple) and once for  $P_L = 0$  (orange). Our results show a clear drop in contrast with increased  $P_H$  for  $P_L = 0$ . For data points using two-power initialization ( $P_L = 6 \mu\text{W}$ ), towards  $P_H \rightarrow 0 \mu\text{W}$ , the low-intensity pulse and our readout laser are responsible for initialization and tend towards 43.5%, similar to the results previously shown [24]. For initialization using solely the combination of readout pulse and high-intensity pulse (orange), we observe a lower contrast optimum around  $P_H = 50 \mu\text{W}$  before dropping to the same contrast given by our reference measurements at  $P_H = 0$ .

We further perform ODMR measurements using the two optimal pulse parameters [Fig. 5(a)]. This was performed with and without two-power initialization, both implemented in the same sequence to guarantee identical external circumstances. It can be seen that the resonance minimum reaches a slightly lower value, while the off-resonant luminescence level is significantly higher, when using two-power initialization. We attribute the increase in photon counts to an improved  $\text{NV}^-$  population caused by the high-power pulse, while the lower minimum additionally underpins the high spin state purity obtained from the low-power pulse.

#### IV. IMPROVEMENT FOR ANY SEQUENCE LENGTH

We find from the model that implementing the two-power initialization sequence is always advantageous in terms of

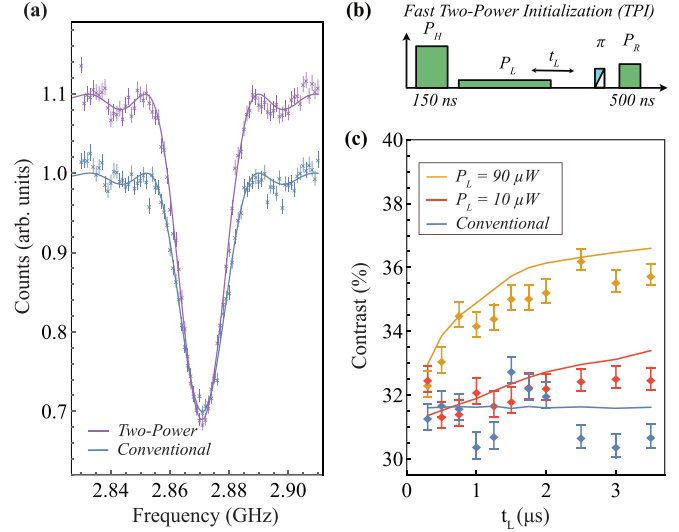


FIG. 5. (a) ODMR measurement performed for two-power initialization using optimized parameters (purple) with  $t_L = 90 \mu\text{s}$  and a readout laser power of 0.9 mW. For comparison a sequence using conventional initialization, where the system is read out using the same laser power as it is initialized with, is shown in blue. Counts are obtained in 280-ns readout windows. Solid lines are  $\text{sinc}^2$  fits to the data. (b) Depiction of the pulse sequence and pulse duration used for high-speed two-power initialization. (c) Contrast obtained from an optimized pulse sequence where the readout pulse is immediately followed by a short (150 ns) high-intensity pulse  $P_H = 21 \text{ mW}$  allowing for rapid charge state initialization. A 200-ns-long pause is inserted for the laser diode to completely switch off before a low-intensity pulse of varying power and length is applied. For a combined initialization and readout duration of 3  $\mu\text{s}$  we already obtain a relative contrast increase of 12% compared with conventional initialization.

measurement sensitivity, independent of the free-evolution time in the measurement sequence (see Appendix D). As an example, a speedup factor of 1.2 is predicted for a free-evolution time of only 500 ns. Confirming this prediction, a measurement sequence with short initialization times is shown in Fig. 5(b). For short evolution times, on the order of microseconds, relevant for recently developed methods such as quantum heterodyne (Qdyne) detection [40], the speedup benefits chiefly from the fast charge state purification using high-power pulses. We observe that the contrast is already improved, compared with conventional initialization, for the shortest measured sequence with an initialization duration of 650 ns. A far greater improvement can be achieved with only a modest increase of the initialization time: A maximal (SNR) contrast of 44% (35%) is already reached with a total combined initialization and readout time of only 3  $\mu\text{s}$  with  $P_L = 90 \mu\text{W}$ ,  $t_L = 2 \mu\text{s}$ , and a readout power of  $P_R = 0.7 \text{ mW}$  [Fig. 5(c)]. For comparison, conventional initialization using this readout power reaches 40.8% (31%) at the readout power used here.

Longer measurement sequences, with a duration of tens to hundreds of microseconds, are regularly used in, e.g., high-resolution magnetometry [23] and the detection of external spins [41,42] using near-surface NV centers [43] or involving the manipulation of nuclear spins [44]. Longer initialization

times can be used in such sequences, which can thereby be accelerated with a speedup factor of  $>1.5$  (see Appendix D).

## V. SUMMARY

In summary, we have shown that a two-power initialization sequence strongly increases the initial spin contrast of the NV center. The improvement persists over the course of the readout duration, giving a contrast increase of  $>17\%$  after 250 ns. The benefit of the sequence is threefold: Firstly, the spin and charge states are initialized with high purity. Secondly, the luminescence collected in the  $NV^-$  spectral window is increased, further improving the SNR. Thirdly, initialization times can be shortened down to only a couple of microseconds while still benefiting from the first two advantages. An additional, though here small, beneficial effect is the observed suppression of background luminescence by bleaching within the detection volume, the nature of which is yet to be determined (see Appendix E). Additionally, we supply a detailed model that is in good agreement with the data recorded here and is able to predict the spin contrast, fluorescence behavior, and time evolution of the system under illumination. The demonstrated method has two requirements: Following a standard readout pulse, a high-power laser pulse is required which must be switched off on a timescale much shorter than the metastable-state lifetime (i.e.,  $\ll 200$  ns). This pulse can be short (on the order of nanoseconds) since the driven shelving pathway does not involve any optical decay processes. Then, a low-power laser pulse with an intensity on the order of 0.5–10% of the readout pulse is needed, the length of which is set by the desired improvement. Both requirements can be fulfilled in most standard NV center experimental setups using acousto-optic modulators or switched laser diodes [24,45].

## VI. DISCUSSION AND CONCLUSION

The two-power initialization method provides a direct route to improved measurements in almost any setting for nitrogen vacancy sensors and can be adapted for a large variety of spin centers [23]. Additionally, the improved initialization may be of use even in low-temperature applications, where accelerated initialization routines for the spin and charge states can reduce the sequence duration [46,47]. The spin readout can be improved further by using a higher readout power than what was available in our experiment. Our model predicts a maximum contrast approaching 48% using two-power initialization, while a (hypothetical) perfect initialization procedure would produce a maximum contrast of slightly above 52%. Finally, we note that the intricate interplay of the spin polarization with the charge state dynamics indicates that the mechanism implemented in this paper will depend on the excitation wavelength [30,48]. This matter underlines the necessity for further investigation, by both theoretical modeling and experimental characterization of the NV center's response to excitation.

## ACKNOWLEDGMENTS

Financial support was provided by Austrian Science Fund (FWF): I 3167-N27 SiC-EiC, FFG QuantERA 864036

Q-Magine, FFG 870002 QSense4Life, and FFG 877615 QSense4Power, as well as the European Union's Horizon 2020 and Horizon Europe research and innovation programs under Projects No. 101038045 (ChemiQS) and No. 101046911 (QuMicro). A.G. acknowledges support from National Research, Development and Innovation Office in Hungary (NKFIH) Grant No. KKP129866 (National Excellence Program) and the EU QuantERA II MAESTRO project. A.G. and V.I. acknowledge support from the Quantum Information National Laboratory sponsored via the Ministry of Culture and Innovation of Hungary. V.I. acknowledges support from the MTA Premium Postdoctoral Research Program and the Knut and Alice Wallenberg Foundation through the WBSQD2 project (Grant No. 2018.0071) and National Research, Development and Innovation Office in Hungary (NKFIH) Grant No. FK 137918. M.N. acknowledges the support from FWO (Funds for Scientific Research) Flanders, Projects No. G0D1721N and No. G0A0520N. M.G. acknowledges Project No. 101038045 (ChemiQS): This project has received funding from the European Union's Horizon 2020 research and innovation program.

## APPENDIX A: MODEL

Having demonstrated the validity of two-power initialization, we aim to explore the effect of charge state conversion on the observed photodynamics of the defect, and infer its effect for higher laser powers. Building upon insights gained from previous work [24,30,49,50], we therefore construct an effective model for the dynamics (see Fig. 1).

We model the negative charge state as a five-level system including two ground states ( $L_1, L_3$ ), two optically excited states ( $L_2, L_4$ ), and one effective singlet state ( $L_7$ ), driven by off-resonant green laser excitation. Levels  $L_5$  and  $L_6$  represent the neutral charge state ( $NV^0$ ). Optically excited  $NV^-$  states can either decay back to the  $NV^-$  ground state via emission of a red photon or decay to the singlet state ( $L_7$ ) via a non-radiative and spin-dependent process. Excitation with green (520 nm) illumination does not supply sufficient energy to directly excite the system from the triplet ground states to the conduction band. Charge state conversion occurs either from the optically excited levels in the triplet manifold of  $NV^-$  [30] or by excitation from the metastable state ( $L_7$ ). The driven channel from  $L_2$  and  $L_4$  takes place via either an Auger process [51] or direct ionization [29] responsible for electron ionization. The former process decays into the ground state of  $NV^0$ , whereas the latter process scatters to the shelving  $^4A_2$  state of  $NV^0$  leaving one electron elevated to the conduction band. The direct photoexcitation can be approximated by an *er* operator, which is a one-body operator. According to the Slater-Condon rules [52,53], only one spin orbital can change in this optical transition; therefore  $^3E$  of  $NV^-$  transforms into  $^4A_2$  of  $NV^0$  plus an electron in the conduction band by photoexcitation. In our experiments we do not find evidence of measurable population of the shelving  $^4A_2$  state; therefore it is ignored in the model. Conversely, the Auger process can be described as swapping two spin orbitals, a two-body operator; therefore  $^3E$  of  $NV^-$  can scatter to the ground state of  $NV^0$  plus an electron high in the conduction band [51].

The photoexcitation of the  ${}^2A_2$  excited state of  $NV^0$  may also occur by either a direct process (promoting an electron from the valence band to the empty  $a_1$  defect level in the gap) or an Auger process (occupying the in-gap  $a_1$  hole by an electron from the in-gap  $e$  level and then promoting an electron from the valence band to the empty  $e$  defect level in the gap). Both processes leave a hole in the valence band. In the direct process, the system arrives at the ground state of  $NV^-$ , i.e.,  $L_6$  goes to the  $L_1$  and  $L_3$  states because of the Slater-Condon principle to which we have alluded. On the other hand, the Auger process enables us to arrive at the metastable state  $L_7$  of  $NV^-$  too, besides the  $L_1$  and  $L_3$  states, where  $L_7$  amalgamates the  ${}^1A_1$  and  ${}^1E$  singlet states because of the very short lifetime of the  ${}^1A_1$  state [54]. The energy cost of these processes varies with the final state. The calculated adiabatic acceptor charge transition level of the NV defect is at about 2.75 eV from the conduction band edge [55,56], whereas the calculated energy gap between the  ${}^3A_2$  ground state and the  ${}^1A_1$  state is at about 1.6 eV (see Ref. [57] and references therein). The total energy cost to convert the  $NV^0$  ground state to the  ${}^1A_1$   $NV^-$  excited state is then about 4.3 eV, which coincides with twice the zero-phonon-line (ZPL) energy of  $NV^0$ . This means that a special excited state of  ${}^1A_1$  of  $NV^-$  binding a hole resonant with the valence band maximum develops. This hole is Coulombically bound, which is a special bound exciton state or Rydberg state which has been observed for the silicon vacancy (SiV) defect [58] and has been recently implied and modeled for the  ${}^3A_2$  plus a bound hole system for the  $NV^-$  defect [59,60]. The bound hole is loosely localized following the effective mass theory. By even taking into account the possible relaxation energy of the ions caused by the change in the electronic states, we may claim that 520-nm laser excitation can reach the  ${}^1A_1$  plus bound hole state of  $NV^-$  by two-photon excitation of  $NV^0$ . Scattering to the  ${}^1E$  ( $L_7$ ) and  ${}^3A_2$  ( $L_1$  and  $L_3$ ) states of  $NV^-$  via an Auger process leaves a hole deep in the valence band at around 1.2 and 1.6 eV from the valence band maximum, respectively. According to our calculation, a resonant  $a_1$  state, broadened by the diamond bands, occurs in this energy region which originates from the dangling bond orbitals of the carbon and nitrogen atoms near the vacant site. Unlike the usual diamond bands that are completely delocalized, the resonant state is weakly localized. This should lead to a larger direct- and Auger-ionization rate of  $NV^0$  than those of  $NV^-$ , because no such high-energy resonant state exists in the conduction band, critical in the photoionization of  $NV^-$ . Previous calculations of the ionization rates of  $NV^-$  implied that the Auger rates are significantly faster than the direct-ionization rates [51]. By asserting the same scenario for the photoionization of  $NV^0$  and considering the resonance condition towards the  ${}^1A_1$  state ( $L_7$ ), we assume a decay from  $L_6$  to  $L_7$  and existing decay channels towards  $L_1$  and  $L_3$ . In this case, the  $NV^-$  ground-state triplet is spin polarized towards the  $m_s = 0$  state. Nevertheless, simulation results could not entirely exclude the possibility that direct ionization to the ground state occurs. In this case, the group theory analysis implies that the population of the  $m_s = 0$  states relative to the  $m_s = \pm 1$  states of  ${}^3A_2$  is given by  $1/3 : 2/3$ .

Furthermore, at high excitation powers, the NV center exhibits nearly power-independent luminescence [33,34].

TABLE I. Model parameters used for the rate equation model.

Parameter	Value
Decay time (ns)	
$\Gamma_{2,1}^{-1}$	13
$\Gamma_{4,3}^{-1}$	13
$\Gamma_{6,5}^{-1}$	20
$\Gamma_{2,7}^{-1}$	93.5(8) <sup>a</sup>
$\Gamma_{4,7}^{-1}$	14.98(6) <sup>a</sup>
$\Gamma_{7,1}^{-1}$	186.12(24) <sup>a</sup>
$\Gamma_{7,3}^{-1}$	2722(57) <sup>a</sup>
Normalized cross section	
$\sigma_{1,2} \equiv \sigma_{3,4}$	1
$\sigma_{7,8}$	0.0059(3) <sup>a</sup>
$\sigma_{6,7}$	0.15(1) <sup>a</sup>
$\sigma_{6,3}$	0.3(2) <sup>a</sup>
$\sigma_{2,5} \equiv \sigma_{4,5}$	0.237(4) <sup>a</sup>
$\sigma_{5,6}$	0.562(7) <sup>a</sup>
$\sigma_{6,1}$	0.281(7) <sup>a</sup>
$L_8$ branching	
$\Gamma_{8,4}/\Gamma_{8,2}$	2.7(1.6) <sup>a</sup>
$\Gamma_{8,5}/\Gamma_{8,2}$	0 <sup>a</sup>
Power scaling (MHz/mW)	
Readout laser	35.0(3) <sup>a</sup>
Initialization laser	25.0(2) <sup>a</sup>

<sup>a</sup>Fitted parameters obtained from the results in the main text.

This behavior is incompatible with perfectly “dark” shelving of the electron in the metastable state, since such a system would display decreasing luminescence towards higher excitation intensity. We therefore include excitation from the metastable ground state ( $L_7$ ) via a single-photon transition to a higher-lying state ( $L_8$ ). A strong and broad transition around 2.58 eV from  ${}^1E$  to  ${}^1E'$  has been observed in numerical simulations and could be excited by 520-nm green illumination (2.384 eV), providing a possible candidate for such a mechanism [35].  ${}^1E'$  can decay to the triplet excited states via an intersystem crossing [57,61]. In the model, decay from  $L_8$  is allowed towards the  $NV^0$  ground state and to the  $NV^-$  triplet excited states, but the numerical optimization converges towards values with negligible decay to the neutral state. We underline that the excitation efficiencies for many of these processes are expected to be strongly wavelength dependent, leading to different dynamics for other excitation energies [48].

The processes described above are collected in a rate equation system where  $\sigma_{i,j}$  denotes the excitation cross section for a transition  $L_i \rightarrow L_j$ , scaled via a variable  $P$  which is globally varied by two free parameters determining laser coupling to the NV center. Since lasers with orthogonal polarization can couple differently to the NV center, we adjust the driving rate constant  $P$  independently for each laser. Similarly, the decay rate from an excited state  $L_e \rightarrow L_g$  is given by  $\Gamma_{e,g}$ . We fix a number of decay rates to literature values, namely,  $\Gamma_{2,1}$ ,  $\Gamma_{4,3}$ , and  $\Gamma_{6,5}$  (see Table I). Furthermore, we fix the lifetime of the higher-lying state ( $L_8$ ) to 200 ps and only vary its relative branching ratios into  $L_1$ ,  $L_3$ , and  $L_5$ . Since not much information about the details of this state is known,

we opted to assign a comparatively fast decay rate to it. This ensures that no population is shelved in this state while its branching still remains included. Our fitted model suggests that this state decays equally into to the optically excited  $m_s = 0$  and  $m_s = \pm 1$  states; however, the obtained error bars leave the possibility of potential spin polarization open. Here, further investigation might be of interest and lead to a better understanding of the optical excitation cycle of the NV center.

Additionally, we fix the excitation cross sections  $\sigma_{3,4} = \sigma_{1,2} = 1$  while all other excitation cross sections are extracted from a numerically optimized fit (see Appendix G) to the data shown in the main text; the excitation cross sections are listed in Table I.

## APPENDIX B: MODEL PREDICTIONS

In this Appendix, we evaluate our model in the high- and low-power excitation regimes, highlighting several features that are of relevance for the measurement of spin-dependent luminescence and photocurrent. The system presents power-dependent shelving due to  $\sigma_{6,7}$ . At low powers, the metastable state will be depopulated predominantly via decay into the triplet ground states ( $\Gamma_{7,1}$  and  $\Gamma_{7,3}$ ). At higher powers, the shelved population is reduced by laser excitation via the transitions with cross section  $\sigma_{7,8}$ . The balance between these processes will define the anomalous saturation, since conversion from  $NV^-$  to  $NV^0$  results in an increase in the shelving rate, while excitation out of the metastable state leads to fluorescence in the high-power limit. These rates also define the photoelectric signal under green illumination and negate the possibility of perfectly protecting nuclear spins from electron decoherence using high-power laser illumination [62].

These mechanisms also explain our improved charge state initialization: Under sufficiently high driving powers, the population will be strongly shelved in  $L_7$ , so long as the excitation rate of the singlet state remains sufficiently small. We find that more than 80% of the population is pumped into the metastable state, such that the charge state error is reduced from 19.5 to 8%. After subsequent relaxation, the shelved population will branch into the  $m_s = \pm 1$  state ( $L_3$ ) with  $R_{7,3} = \Gamma_{7,3}/(\Gamma_{7,1} + \Gamma_{7,3}) = 0.07$  and into the  $m_s = 0$  state ( $L_1$ ) with  $R_{7,1} = \Gamma_{7,1}/(\Gamma_{7,1} + \Gamma_{7,3}) = 0.93$  (see Table I). A high-intensity pulse thus initializes the charge state effectively, at the cost of spin polarization within the  $NV^-$  manifold.

At this point, the  $m_s = 0$  population can, however, be increased using weak laser excitation: In the low-power limit, where  $P\sigma_{2,5} \ll \Gamma_{2,1} + \Gamma_{2,7}$  and  $P\sigma_{4,5} \ll \Gamma_{4,3} + \Gamma_{4,7}$ , the rate of transfers between charge states is negligible. It is therefore possible to initialize the spin state effectively within the  $NV^-$  subsystem in this regime, via the decay rate ratios  $\Gamma_{4,7}/\Gamma_{2,7} > 1$  and  $\Gamma_{7,1}/\Gamma_{7,3} > 1$ . The  $m_s = 0$  population can then be increased to a maximum of  $1/(1 + R_{2,7}\Gamma_{7,3}/R_{4,7}\Gamma_{7,1}) = 98\%$  within the  $NV^-$  manifold, where  $R_{2,7} = \Gamma_{2,7}/(\Gamma_{2,1} + \Gamma_{2,7})$  and  $R_{4,7} = \Gamma_{4,7}/(\Gamma_{4,3} + \Gamma_{4,7})$ , respectively. Since time is a limiting factor in measurements, in practice the achievable spin polarization will be the result of a compromise between expediency and charge state conversion probability.

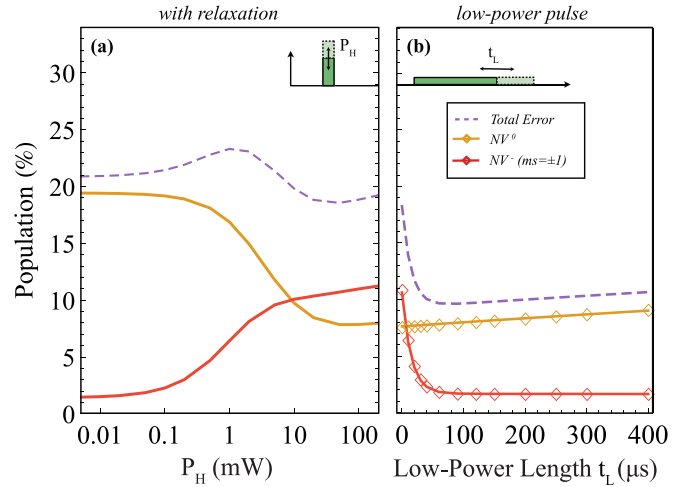


FIG. 6. (a) Population after relaxation from the steady state for continuous-wave illumination with intensity  $P_H$ . High-power illumination leads to shelving in the metastable state, which permits high-fidelity charge state initialization. The  $NV^0$  population (orange) decreases towards high pumping power  $P_H \gg 1$  mW, but the  $m_s = \pm 1$  population (red) increases. The sum of these populations gives the total initialization error (dashed line). (b) Model evaluation of spin state error within  $NV^-$  (portion of total population in  $m_s = \pm 1$ ), charge state error (population in  $NV^0$ ), and total error (sum of both, purple) under low-power initialization after a 21-mW initialization pulse. The diamonds are obtained from low-power approximations (see main text), which coincide well with the full model at low excitation powers.

The key mechanisms are summarized in Fig. 6. Figure 6(a) shows the calculated populations for  $NV^0$  (orange) and  $m_s = \pm 1$  (red) for relaxation after a long pulse of a given power, i.e., after relaxation from the steady state. The dashed purple line is the total initialization error calculated by taking the sum of both. While in the low-power regime we obtain a constant  $NV^0$  population of about 19.5%, in agreement with the findings in Ref. [30], increasing the power beyond 1 mW will initialize the charge state towards  $NV^-$  while simultaneously worsening the  $NV^-$  spin state initialization. Figure 6(b) shows the effect of subsequent spin initialization using low intensity versus time (solid lines). It can be seen that this second pulse rapidly reduces the spin error caused by the charge state pulse. For long illumination times, the error increases again due to slow charge state conversion of the NV center. We find that for low powers this rate can be approximated as  $P^2\sigma_{1,2}\sigma_{2,5}/(\Gamma_{2,1} + \Gamma_{2,7})$  and the polarization rate can be approximated as  $P\sigma_{1,2}R_{4,7}R_{7,1}$ . Conversely, the  $NV^0$  to  $NV^-$  charge recapture can be approximated as  $P^2\sigma_{5,6}\sigma_{6,7}/\Gamma_{6,5}$ . The results obtained from these approximations are indicated by the diamonds in Fig. 6(b). The resulting luminescence contrast and the spin polarization are both highly dependent on the parameters assumed for the branching ratios in the excited and metastable states. In Table II, we compare selected values from the literature, cautioning that the assumptions, measurement methods, and experimental settings were rather different in each case. For each set, we also show the calculated initial contrast achievable for perfect spin and charge state initialization, as well as only for perfect charge state initialization.



TABLE II. Comparison of selected and literature parameters. The first two columns of data show the maximal  $m_s = 0$  and  $m_s = \pm 1$  populations ( $L_0$ ,  $L_1$ ) in the low-power limit. Since the selected literature models do not include both charge states of the NV center, in the ‘‘Chosen’’ row we state two values for respective  $L_0(\text{max})$  and  $L_1(\text{max})$  populations: The first value assumes no charge mixing, for which comparatively high spin initialization is obtained; values in parentheses, instead, give the resulting population taking the neutral charge state into account. The next three columns show the metastable state branching ratio (MS) towards the optical ground state as well as the branching ratios of the optically excited  $\text{NV}^-$  states (E0,  $E\pm 1$ ). Furthermore, using these values, in the last two columns we calculate the maximal initial contrast ( $L_0 = 1$ ), for which we assume perfect  $m_s = 0$  initialization, as well as the spin readout contrast obtained from the maximally achievable  $m_s = 0$  initialization; we note that these values are lower than what we obtained in our measurements since, in order to allow for comparison between literature values, they are calculated as  $C = 1 - \frac{L_0 R_{4,3} + L_1 R_{2,1} + 0.6 L_5}{L_1 R_{4,3} + L_0 R_{2,1} + 0.6 L_5}$ , where the factor 0.6 stems from the spectral selectivity of  $\text{NV}^0$ .

	Population		Branching ratio			Contrast	
	$L_0(\text{max})$	$L_1(\text{max})$	MS( $R_{7,1}$ )	E0( $R_{2,7}$ )	$E\pm 1$ ( $R_{4,7}$ )	$L_0 = 1$	$L_0(\text{max})$
Tetienne <i>et al.</i> [63]	0.88	0.12	0.57	0.09	0.41	0.38	0.3
Gupta <i>et al.</i> [64]	0.91	0.09	0.7	0.13	0.57	0.51	0.44
Kalb <i>et al.</i> [65]	1	0	0.8	0	0.41	0.39	0.39
Thiering and Gali [66]			0.84				
Chosen	0.98 (0.79)	0.017 (0.014)	0.93	0.12	0.46	0.39	0.33

### APPENDIX C: LUMINESCENCE SIGNAL

The maximum contrast and the contrast at the best signal-to-noise ratio (SNR) for spin-dependent luminescence measurements can be extracted from the time-dependent state occupations under pulsed excitation and are shown in Fig. 7. Firstly, we evaluate the dynamics of the system under the assumption that the populations have reached a steady state after illumination with laser intensity  $P_R$  (scenario I in Fig. 7). This equilibrium is usually reached even after a few short measurement pulses on the order of approximately microseconds,

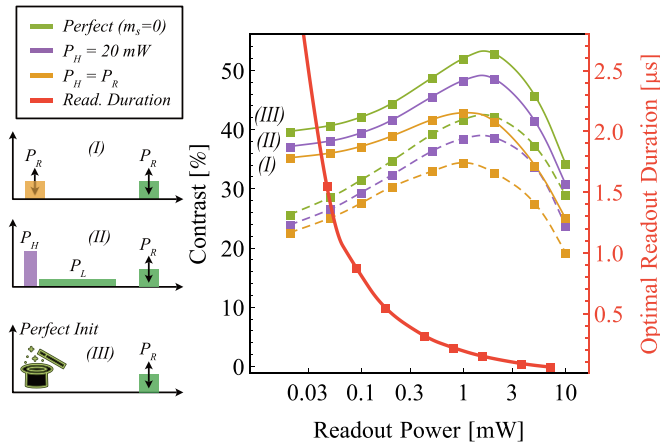


FIG. 7. Readout power. Model contrast predictions under variation of readout power for three cases (scenarios I–III). Green lines show the result if the system could be perfectly initialized into  $m_s = 0$ . Purple lines correspond to a charge state pulse of 20 mW, i.e., the value with the best expected performance in our data, followed by a low-intensity pulse of  $6 \mu\text{W}$  for  $90 \mu\text{s}$ . Orange lines show the conventional sequence used in experiments, where the readout pulse is of the same power as the initialization pulse. Solid lines show the maximal contrast obtained at a singular point within the readout duration, while the dashed lines show the SNR contrast (for maximum SNR), found by optimizing the readout duration (red line). Read., readout; Init, initialization.

and should therefore correctly depict common experimental conditions. Furthermore, it is necessary to consider the relative signal strengths for the luminescence of the two charge states, which cannot be perfectly discriminated by spectral filtering. In the experiment, we use a long-pass filter with an edge wavelength of 650 nm. From the filter transmission and the spectral properties of the two charge states [59], we estimate a spectral selectivity of  $\text{NV}^0$  relative to  $\text{NV}^-$  of 0.6 : 1. The combined luminescence signal of the two charge states is thus calculated from the bright transition rates  $S = L_2 \Gamma_{2,1} + L_4 \Gamma_{4,3} + 0.6 \times L_6 \Gamma_{6,5}$ .

In order to extract the contrast, we use two input states: In the first case, the population distributions after initialization are taken as the initial conditions, resulting in the signal  $S_0$ . In the second case, the  $L_1$  population is fully swapped with the  $L_3$  population, corresponding to a  $\pi$  rotation of the initialized state from  $m_s = 0$  to  $m_s = \pm 1$ , resulting in the signal  $S_1$ . The optimal measurement time is then found by numerical integration of the two signals over the readout time to maximize the quantity  $\text{SNR} = (S_0 - S_1) / \sqrt{S_0 + S_1}$ .

We examine two further initialization conditions. In scenario II, the starting conditions are chosen to match the population resulting from the two-step initialization sequence described in the main text with  $P = 20 \text{ mW}$  and  $t_L = 90 \mu\text{s}$ . This choice improves both the maximal contrast and the best-SNR contrast significantly, reaching values of 48 and 38%, respectively. Green lines show the upper contrast limit predicted by our model in scenario III, where perfect initialization into  $m_s = 0$  is assumed. We make the simplifying assumption that the excitation light causes no extraneous background scattering.

In summary, the two-step initialization procedure, combined with an optimized readout intensity, provides a remarkable improvement in the signal difference that can be extracted from a spin-dependent measurement. Our model furthermore predicts that, with further improvements to the initialization, a peak contrast of almost 52% (best SNR: 41%) could be reached by perfect spin and charge state initialization.

## APPENDIX D: EFFICIENCY

Two-power initialization can effectively increase the readout contrast by more than  $\sim 17\%$  and boost the peak photon count rate by 11% (see main text). We will follow up with an analysis of the expected speedups gained from using three separate laser powers for readout and initialization and compare our results with the conventionally used method of using a single pulse for readout and initialization. High-power illumination will lead to an initial reduction in readout contrast compared with the commonly used method due to the inferior branching ratio of the metastable state (see previous sections and main text). However, for the high-intensity pulse  $P_H$ , only very short times are necessary since, according to our model, it only relies on driven channels which are not delayed by any decay time. Here we expect a trade-off between expediency and initialization quality to occur. Conversely, the low-intensity pulse  $P_L$  must be sufficiently weak in order to avoid charge state conversion. This requirement, in turn, can lead to long (many-microsecond) pulses for the spin polarization to take effect. In order to obtain a break-even point that optimizes the applied initialization for a given manipulation time  $\tau_M$ , we compare three different initialization methods with respect to their sensitivities. We follow the treatment of Ref. [23], where the sensitivity is given by

$$\eta \sim \frac{\sqrt{\tau_I + \tau_M}}{\sqrt{N}} \frac{1}{C_{\text{opt}}} \frac{1}{\tau_M} \frac{1}{e^{-\tau_M/T_2^*}}. \quad (\text{D1})$$

Here,  $T_2^*$  corresponds to the dephasing time,  $\tau_M$  and  $\tau_I$  represent the time necessary for manipulation and initialization, respectively,  $C_{\text{opt}} = (S_1 - S_0)/(S_1 + S_0)$  is the readout contrast, and  $N$  is the average number of photons collected per sequence.

We numerically solve our model for three cases: Readout-pulse initialization (RPI) is the commonly employed method, where a laser pulse with power  $P_R$  and duration  $\tau_R$  provides both readout and initialization. Single-pulse initialization (SPI) includes a second, weaker pulse of power  $P_L$  and length  $\tau_L$  for initialization; thus different powers are allowed for readout and initialization. For two-power initialization (TPI), we include a short, high-intensity pulse ( $P_H, \tau_H$ ). We furthermore include a pause  $\tau_p$  after each initialization sequence, so that metastable state decay into the  $\text{NV}^-$  optical ground state can take place. Additionally, we define the system as “initialized” if, independently of the starting state, the system always ends up in the same final state (up to a 0.1% error). The total initialization time is then calculated as  $\tau_I = \tau_R + \tau_H + \tau_L + \tau_p$  and optimized for all manipulation lengths,  $\tau_M$ . Since we compare the three cases for identical spin manipulation times, the factor  $\tau_M \exp(\tau_M/T_2^*)$  drops out in the calculation.

To obtain the speedup provided by our improved initialization sequence, we compare readout-pulse initialization with single- and two-power sequences using

$$\frac{T_{(\text{SPI}) \text{ or } (\text{TPI})}}{T_{\text{RPI}}} = \frac{\eta_{(\text{SPI}) \text{ or } (\text{TPI})}^2}{\eta_{\text{RPI}}^2}, \quad (\text{D2})$$

where  $\eta$  corresponds to the sensitivity of the respective initialization method at a fixed manipulation time  $\tau_M$  and  $T$  is

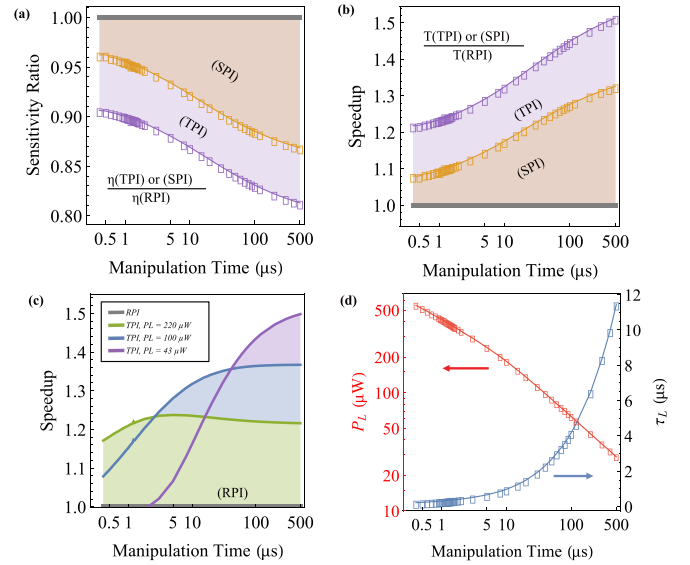


FIG. 8. Speedup. (a) We optimize the sensitivity for RPI, SPI, and TPI for a set of manipulation times to obtain the sensitivity gain. All parameters are left free during optimization though we force the application of a 20-ns-long high-power (30 mW) pulse for TPI. Both SPI and TPI prove beneficial for all manipulation lengths. (b) Predicted speedup in measurement time. (c) Comparison of the sensitivity for four selected cases: readout-pulse initialization with  $P_R = 1$  mW (gray) and two-power initialization (TPI) for  $P_R = 1$  mW and fixed  $P_L = 380 \mu\text{W}$  (green),  $P_L = 200 \mu\text{W}$  (blue), and  $P_L = 43 \mu\text{W}$  (purple). With these fixed values we only allow  $\tau_L$  to vary. (d) Optimal  $P_L$  and  $\tau_L$  for all sets of manipulation times using TPI (we note that SPI leads to very similar results).

calculated as  $T = \eta^2$  and represents the time necessary to reach a certain SNR.

The results are depicted in Fig. 8 showing the scaled sensitivities for RPI and three cases of TPI. We obtain an immediate improvement in sensitivity for both SPI and TPI. The benefit from SPI shows that initialization and readout should in general be performed at different powers due to power-dependent charge state conversion. The benefit of TPI stems from the fast state initialization at high powers. While a single readout pulse typically needs about 1–2 μs to properly initialize the system, usually only the first 300 ns are of interest for signal acquisition. Using TPI on the other hand, the readout pulse can be kept short (300 ns), while subsequent application of the high-power pulse only needs about 20 ns to reach a steady state. The spin state error resulting from high-power initialization (see main text) is, however, outweighed by the comparatively fast initialization. For long manipulation times an increasing amount of time can be spent to repair the resulting spin error using subsequent low-power illumination without a significant increase in sequence length. Sensitivity for TPI thus gets monotonically better since the low-power pulse can be kept at lower and lower powers while increasing its length to avoid charge state mixing. Figure 8(b) shows the predicted speedup for TPI and SPI. Furthermore, Fig. 8(c) shows the achieved speedup for three selected low-power pulses. While the previous results were obtained by optimization of pulse lengths and powers, here we fix the readout power  $P_R = 1$  mW, and  $P_L = \{43 \mu\text{W}, 200 \mu\text{W}, 380 \mu\text{W}\}$

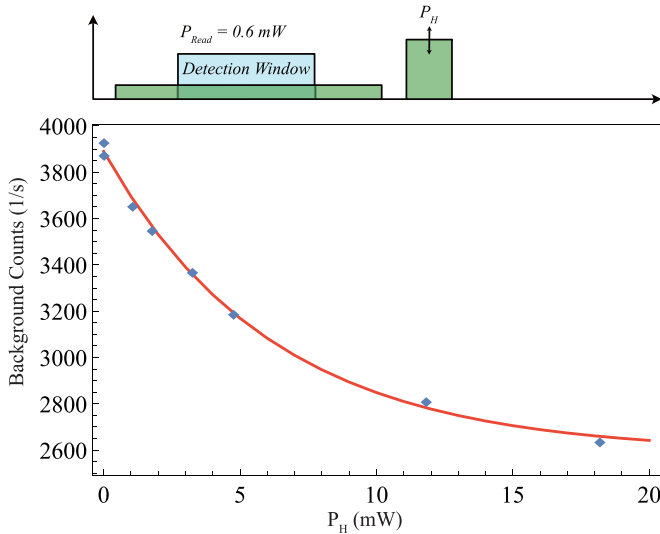


FIG. 9. Background counts taken  $3\ \mu\text{m}$  away from the NV center during a constant  $0.6\text{-mW}$  readout pulse when followed by an additional  $5\text{-}\mu\text{s}$ -long pulse with varying  $P_H$ . During these measurements, as in all data captured in the main text, we kept the total sequence length at  $100\ \mu\text{s}$  in order to maintain identical circumstances. We obtain an exponential reduction from  $\sim 3900$  counts per second to  $\sim 2700$  counts per second with increasing  $P_H$ . For comparison, at  $0.6\ \text{mW}$  we collect about  $7 \times 10^4$  counts per second when focused on the NV center. We attribute the reduced fluorescence to a background signal that is bleached away by increasing illumination intensity.

while we numerically optimize the low-power pulse length at these instances [Fig. 8(c)]. For short manipulation times, it proves beneficial to apply short, comparatively strong pulses ( $380\ \mu\text{W}$ ) at the end of the initialization step instead of long, e.g.,  $43\text{-}\mu\text{W}$ , pulses since low-power pulses require more time for proper initialization. For long manipulation times, however, we obtain a speedup surpassing 1.5. Figure 8(d) shows the numerically calculated optimal powers and pulse lengths for the low-power pulse in TPI. We note that the optimal  $P_L$  and  $\tau_L$  for SPI derived from our model are almost identical to those for TPI.

#### APPENDIX E: BACKGROUND SUBTRACTION

During all measurements, we observed a slight increase of 2% in the reference contrast from steps II and IV (see main text, Fig. 3(a)) when the high-intensity pulse was added to the TPI sequence (steps I and III). We thus performed a set of background measurements using the two-power initialization sequence while varying the power of the high-intensity pulse (Fig. 9). These measurements were performed by collecting fluorescence  $3\ \mu\text{m}$  away from the NV center on a spot without any other NV centers at the same depth. We observed a clear decrease in collected background photons with increasing  $P_H$ , which we attribute to unwanted fluorescence that is bleached away by the additional pulse. We thus corrected our photon count rates using  $P_H$ -dependent background counts.

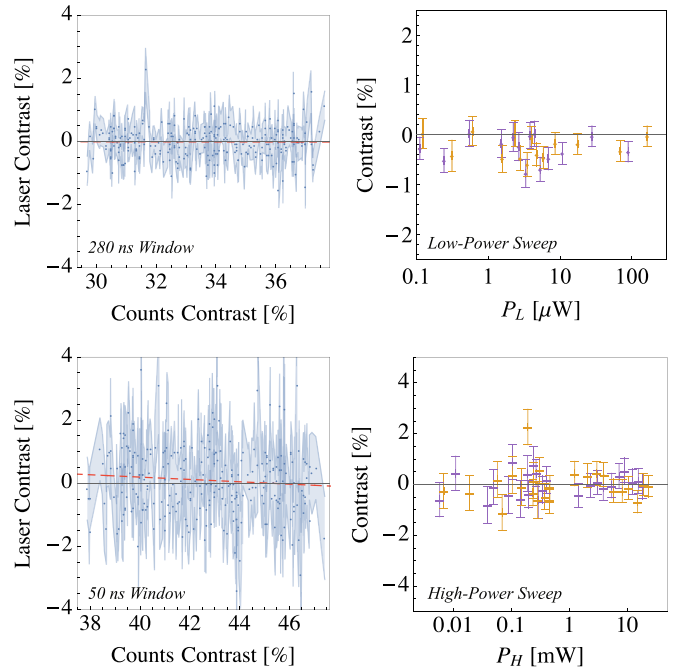


FIG. 10. Laser contrast correlations. We perform a contrast calculation on the laser power traces recorded using a separate photon counter. The data processing is identical to that used for the evaluation of NV center photoluminescence counts. Left plots: The contrast that could stem from laser diode fluctuations vs the contrast from each data point for both long (top) and short (bottom) integration windows. Red lines in the plots show a linear fit through all points. Right plots: Contrast of our data sets that sweep  $P_H$  and  $P_L$  when applied to the laser traces.

#### APPENDIX F: LASER CHARACTERISTICS

As described in the main text, we use two laser diodes driven directly by a TTL-switchable diode driver for readout and high- or low-intensity pulses, respectively. This separation prevents potential correlations caused by laser diode characteristics. As an example, driving a diode at peak power can cause intensity variations in subsequent pulses due to electronic or thermal effects. We stress that the use of two laser diodes is not a requirement for the improved initialization and was only implemented to guarantee highly repeatable readout pulses for a broad variation of initialization pulse characteristics.

In order to quantify the effects of laser fluctuations on our results, we sampled part of the excitation light into a fiber to record the laser time traces during the experiments described in the main text. We applied all contrast calculations to our fluorescence traces (main text) as well as to the recorded laser traces. Figure 10 shows the obtained contrast from the laser versus the contrasts resulting from our fluorescence traces (left panels) for both short and long integration windows. While for short integration windows we see a very slight anti-correlation (red lines), we observe no correlation between the two quantities for longer integration windows. We additionally apply our contrast calculation to the  $P_H$  and  $P_L$  sweeps. These also show no significant correlation, proving that laser pulse variability does not contribute to the observed contrast improvements.

### APPENDIX G: NUMERICAL OPTIMIZATION AND GENETIC ALGORITHM

In order to fit our free parameters to the experimental results, we numerically solve the system matrix to retrieve time traces for each data measurement trace. Those traces consist of the first 500 ns of each readout pulse for both readout power initialization and two-power initialization. Our optimization parameter is obtained by finding the least-squares deviation of the simulated fluorescence relative to the measured fluorescence. Additionally, we compare the fluorescence of our model during stepwise increase of continuous laser excitation power to a measured fluorescence. The sum of both is calculated to obtain the total fit error  $\Delta_{\text{opt}}$ . We further give an abstract overview of the optimization process: We first create a parent state vector  $P_1 = (A_1, A_2, \dots, A_n) = (\Gamma_1, \dots, \Gamma_j, \sigma_1, \dots, \sigma_k)$  for which we can evaluate  $\Delta_{\text{opt}}$ . We additionally create a second parent  $P_2$  that contains randomized elements. Both parents are used to create three offspring members  $O_{1,2,3}$  via random cutting and swapping. Below we describe the procedure using a seven-parameter space. Offspring creation then leads to

$$\begin{aligned}
 P_1 &= \begin{bmatrix} A_1 \\ A_2 \\ A_3 \\ A_4 \\ A_5 \\ A_6 \\ A_7 \end{bmatrix}, & P_2 &= \begin{bmatrix} B_1 \\ B_2 \\ B_3 \\ B_4 \\ B_5 \\ B_6 \\ B_7 \end{bmatrix} \\
 \rightarrow O_1 &= \begin{bmatrix} B_1 \\ B_2 \\ A_3 \\ A_4 \\ A_5 \\ A_6 \\ A_7 \end{bmatrix}, & O_2 &= \begin{bmatrix} A_1 \\ A_2 \\ A_3 \\ A_4 \\ A_5 \\ A_6 \\ B_7 \end{bmatrix}, & O_3 &= \begin{bmatrix} B_1 \\ B_2 \\ B_3 \\ B_4 \\ A_5 \\ A_6 \\ A_7 \end{bmatrix}.
 \end{aligned} \tag{G1}$$

Offspring vectors are then mutated such that each parameter has a probability of changing by a random factor  $\delta_i \in [1 - \epsilon, 1 + \epsilon]$ , e.g.,  $\tilde{A}_3 = \delta_3 A_3$ . We give all elements of each offspring member a 20% chance of mutation. From this procedure we obtain, e.g., the set

$$\begin{aligned}
 P_1 &= \begin{bmatrix} A_1 \\ A_2 \\ A_3 \\ A_4 \\ A_5 \\ A_6 \\ A_7 \end{bmatrix}, & P_2 &= \begin{bmatrix} B_1 \\ B_2 \\ B_3 \\ B_4 \\ B_5 \\ B_6 \\ B_7 \end{bmatrix}, \\
 O_1 &= \begin{bmatrix} \tilde{B}_1 \\ B_2 \\ \tilde{A}_3 \\ \tilde{A}_4 \\ A_5 \\ A_6 \\ A_7 \end{bmatrix}, & O_2 &= \begin{bmatrix} \tilde{A}_1 \\ \tilde{A}_2 \\ A_3 \\ \tilde{A}_4 \\ A_5 \\ A_6 \\ B_7 \end{bmatrix}, & O_3 &= \begin{bmatrix} B_1 \\ \tilde{B}_2 \\ B_3 \\ B_4 \\ A_5 \\ A_6 \\ \tilde{A}_7 \end{bmatrix},
 \end{aligned} \tag{G2}$$

for which we evaluate all individual  $\Delta_{\text{opt}}$ , then select the two that minimize  $\Delta_{\text{opt}}$  best, which are chosen as new parents from which the process repeats. Finally, we note that in the actual optimization process, six offspring members were created from each set of parents, and the parameter space consisted of all free parameters.

- 
- [1] M. W. Doherty, N. B. Manson, P. Delaney, F. Jelezko, J. Wrachtrup, and L. C. L. Hollenberg, The nitrogen-vacancy colour centre in diamond, *Phys. Rep.* **528**, 1 (2013).
  - [2] L. Rondin, J. P. Tetienne, T. Hingant, J. F. Roch, P. Maletinsky, and V. Jacques, Magnetometry with nitrogen-vacancy defects in diamond, *Rep. Prog. Phys.* **77**, 056503 (2014).
  - [3] G. Kucsko, P. C. Maurer, N. Y. Yao, M. Kubo, H. J. Noh, P. K. Lo, H. Park, and M. D. Lukin, Nanometre-scale thermometry in a living cell, *Nature (London)* **500**, 54 (2013).
  - [4] F. Dolde, H. Fedder, M. W. Doherty, T. Nöbauer, F. Rempp, G. Balasubramanian, T. Wolf, F. Reinhard, L. C. L. Hollenberg, F. Jelezko, and J. Wrachtrup, Electric-field sensing using single diamond spins, *Nat. Phys.* **7**, 459 (2011).
  - [5] P. Neumann, I. Jakobi, F. Dolde, C. Burk, R. Reuter, G. Waldherr, J. Honert, T. Wolf, A. Brunner, J. H. Shim, D. Suter, H. Sumiya, J. Isoya, and J. Wrachtrup, High-precision nanoscale temperature sensing using single defects in diamond, *Nano Lett.* **13**, 2738 (2013).
  - [6] L. J. Rogers, K. D. Jahnke, M. W. Doherty, A. Dietrich, L. P. McGuinness, C. Müller, T. Teraji, H. Sumiya, J. Isoya, N. B. Manson, and F. Jelezko, Electronic structure of the negatively charged silicon-vacancy center in diamond, *Phys. Rev. B* **89**, 235101 (2014).
  - [7] J. N. Becker, J. Görlitz, C. Arend, M. Markham, and C. Becher, Ultrafast all-optical coherent control of single silicon vacancy colour centres in diamond, *Nat. Commun.* **7**, 13512 (2016).
  - [8] A. Sipahigil, R. E. Evans, D. D. Sukachev, M. J. Burek, J. Borregaard, M. K. Bhaskar, C. T. Nguyen, J. L. Pacheco, H. A. Atikian, C. Meuwly, R. M. Camacho, F. Jelezko, E. Bielejec, H. Park, M. Lončar, and M. D. Lukin, An integrated diamond nanophotonics platform for quantum-optical networks, *Science* **354**, 847 (2016).
  - [9] D. J. Christle, A. L. Falk, P. Andrich, P. V. Klimov, J. U. Hassan, N. T. Son, E. Janzén, T. Ohshima, and D. D. Awschalom, Isolated electron spins in silicon carbide with millisecond coherence times, *Nat. Mater.* **14**, 160 (2015).

- [10] M. Widmann, S.-Y. Lee, T. Rendler, N. T. Son, H. Fedder, S. Paik, L.-P. Yang, N. Zhao, S. Yang, I. Booker, A. Denisenko, M. Jamali, S. A. Momenzadeh, I. Gerhardt, T. Ohshima, A. Gali, E. Janzén, and J. Wrachtrup, Coherent control of single spins in silicon carbide at room temperature, *Nat. Mater.* **14**, 164 (2015).
- [11] F. Fuchs, B. Stender, M. Trupke, D. Simin, J. Pflaum, V. Dyakonov, and G. V. Astakhov, Engineering near-infrared single-photon emitters with optically active spins in ultrapure silicon carbide, *Nat. Commun.* **6**, 7578 (2015).
- [12] T. Bosma, G. J. J. Lof, C. M. Gilardoni, O. V. Zwier, F. Hendriks, B. Magnusson, A. Ellison, A. Gällström, I. G. Ivanov, N. T. Son, R. W. A. Havenith, and C. H. van der Wal, Identification and tunable optical coherent control of transition-metal spins in silicon carbide, *npj Quantum Inf.* **4**, 48 (2018).
- [13] G. Wolfowicz, F. J. Heremans, C. P. Anderson, S. Kanai, H. Seo, A. Gali, G. Galli, and D. D. Awschalom, Quantum guidelines for solid-state spin defects, *Nat. Rev. Mater.* **6**, 906 (2021).
- [14] M. Pfender, N. Aslam, P. Simon, D. Antonov, G. Thiering, S. Burk, F. Fávoro de Oliveira, A. Denisenko, H. Fedder, J. Meijer, J. A. Garrido, A. Gali, T. Teraji, J. Isoya, M. W. Doherty, A. Alkauskas, A. Gallo, A. Grüneis, P. Neumann, and J. Wrachtrup, Protecting a diamond quantum memory by charge state control, *Nano Lett.* **17**, 5931 (2017).
- [15] B. J. Shields, Q. P. Unterreithmeier, N. P. de Leon, H. Park, and M. D. Lukin, Efficient Readout of a Single Spin State in Diamond via Spin-to-Charge Conversion, *Phys. Rev. Lett.* **114**, 136402 (2015).
- [16] M. Gulka, E. Bourgeois, J. Hruby, P. Siyushev, G. Wachter, F. Aumayr, P. R. Hemmer, A. Gali, F. Jelezko, M. Trupke, and M. Nesladek, Pulsed Photoelectric Coherent Manipulation and Detection of N–V Center Spins in Diamond, *Phys. Rev. Appl.* **7**, 044032 (2017); **7**, 069901(E) (2017).
- [17] E. Bourgeois, A. Jarmola, P. Siyushev, M. Gulka, J. Hruby, F. Jelezko, D. Budker, and M. Nesladek, Photoelectric detection of electron spin resonance of nitrogen-vacancy centres in diamond, *Nat. Commun.* **6**, 8577 (2015).
- [18] P. Siyushev, M. Nesladek, E. Bourgeois, M. Gulka, J. Hruby, T. Yamamoto, M. Trupke, T. Teraji, J. Isoya, and F. Jelezko, Photoelectrical imaging and coherent spin-state readout of single nitrogen-vacancy centers in diamond, *Science* **363**, 728 (2019).
- [19] M. Gulka, D. Wirtitsch, V. Ivády, J. Vodnik, J. Hruby, G. Magchiels, E. Bourgeois, A. Gali, M. Trupke, and M. Nesladek, Room-temperature control and electrical readout of individual nitrogen-vacancy nuclear spins, *Nat. Commun.* **12**, 4421 (2021).
- [20] F. M. Stürner, A. Brenneis, J. Kassel, U. Wostradowski, R. Roelver, T. Fuchs, K. Nakamura, H. Sumiya, S. Onoda, J. Isoya, and F. Jelezko, Compact integrated magnetometer based on nitrogen-vacancy centres in diamond, *Diamond Relat. Mater.* **93**, 59 (2019).
- [21] D. Kim, M. I. Ibrahim, C. Foy, M. E. Trusheim, R. Han, and D. R. Englund, A CMOS-integrated quantum sensor based on nitrogen–vacancy centres, *Nat. Electron* **2**, 284 (2019).
- [22] J. L. Webb, J. D. Clement, L. Troise, S. Ahmadi, G. J. Johansen, A. Huck, and U. L. Andersen, Nanotesla sensitivity magnetic field sensing using a compact diamond nitrogen-vacancy magnetometer, *Appl. Phys. Lett.* **114**, 231103 (2019).
- [23] J. F. Barry, J. M. Schloss, E. Bauch, M. J. Turner, C. A. Hart, L. M. Pham, and R. L. Walsworth, Sensitivity optimization for NV-diamond magnetometry, *Rev. Mod. Phys.* **92**, 015004 (2020).
- [24] Y. Song, Y. Tian, Z. Hu, F. Zhou, T. Xing, D. Lu, B. Chen, Y. Wang, N. Xu, and J. Du, Pulse-width-induced polarization enhancement of optically pumped N-V electron spin in diamond, *Photonics Res.* **8**, 1289 (2020).
- [25] D. A. Hopper, J. D. Lauigan, T.-Y. Huang, and L. C. Bassett, Real-Time Charge Initialization of Diamond Nitrogen-Vacancy Centers for Enhanced Spin Readout, *Phys. Rev. Appl.* **13**, 024016 (2020).
- [26] Z. Mu, S. A. Zargaleh, H. J. von Bardeleben, J. E. Fröch, M. Nonahal, H. Cai, X. Yang, J. Yang, X. Li, I. Aharonovich, and W. Gao, Coherent manipulation with resonant excitation and single emitter creation of nitrogen vacancy centers in 4H silicon carbide, *Nano Lett.* **20**, 6142 (2020).
- [27] J.-F. Wang, F.-F. Yan, Q. Li, Z.-H. Liu, H. Liu, G.-P. Guo, L.-P. Guo, X. Zhou, J.-M. Cui, J. Wang, Z.-Q. Zhou, X.-Y. Xu, J.-S. Xu, C.-F. Li, and G.-C. Guo, Coherent Control of Nitrogen-Vacancy Center Spins in Silicon Carbide at Room Temperature, *Phys. Rev. Lett.* **124**, 223601 (2020).
- [28] S. Felton, A. M. Edmonds, M. E. Newton, P. M. Martineau, D. Fisher, and D. J. Twitchen, Electron paramagnetic resonance studies of the neutral nitrogen vacancy in diamond, *Phys. Rev. B* **77**, 081201(R) (2008).
- [29] L. Razinkovas, M. Maciaszek, F. Reinhard, M. W. Doherty, and A. Alkauskas, Photoionization of negatively charged NV centers in diamond: Theory and *ab initio* calculations, *Phys. Rev. B* **104**, 235301 (2021).
- [30] N. Aslam, G. Waldherr, P. Neumann, F. Jelezko, and J. Wrachtrup, Photo-induced ionization dynamics of the nitrogen vacancy defect in diamond investigated by single-shot charge state detection, *New J. Phys.* **15**, 013064 (2013).
- [31] S. Baier, C. E. Bradley, T. Middelburg, V. V. Dobrovitski, T. H. Taminiau, and R. Hanson, Orbital and Spin Dynamics of Single Neutrally-Charged Nitrogen-Vacancy Centers in Diamond, *Phys. Rev. Lett.* **125**, 193601 (2020).
- [32] R. P. Roberts, M. L. Juan, and G. Molina-Terriza, Spin-dependent charge state interconversion of nitrogen vacancy centers in nanodiamonds, *Phys. Rev. B* **99**, 174307 (2019).
- [33] K. Y. Han, D. Wildanger, E. Rittweger, J. Meijer, S. Pezzagna, S. W. Hell, and C. Eggeling, Dark state photophysics of nitrogen–vacancy centres in diamond, *New J. Phys.* **14**, 123002 (2012).
- [34] R. Chapman and T. Plakhotnik, Anomalous saturation effects due to optical spin depolarization in nitrogen-vacancy centers in diamond nanocrystals, *Phys. Rev. B* **86**, 045204 (2012).
- [35] M. Bockstedte, F. Schütz, T. Garratt, V. Ivády, and A. Gali, Ab initio description of highly correlated states in defects for realizing quantum bits, *npj Quantum Mater.* **3**, 31 (2018).
- [36] X.-D. Chen, L.-M. Zhou, C.-L. Zou, C.-C. Li, Y. Dong, F.-W. Sun, and G.-C. Guo, Spin depolarization effect induced by charge state conversion of nitrogen vacancy center in diamond, *Phys. Rev. B* **92**, 104301 (2015).
- [37] G. Waldherr, Y. Wang, S. Zaiser, M. Jamali, T. Schulte-Herbrüggen, H. Abe, T. Ohshima, J. Isoya, J. F. Du, P. Neumann, and J. Wrachtrup, Quantum error correction in a solid-state hybrid spin register, *Nature (London)* **506**, 204 (2014).
- [38] V. Jacques, P. Neumann, J. Beck, M. Markham, D. Twitchen, J. Meijer, F. Kaiser, G. Balasubramanian, F. Jelezko, and J.

- Wrachtrup, Dynamic Polarization of Single Nuclear Spins by Optical Pumping of Nitrogen-Vacancy Color Centers in Diamond at Room Temperature, *Phys. Rev. Lett.* **102**, 057403 (2009).
- [39] This relates to the fringe contrast commonly used in, e.g., optics,  $C_{\text{opt}} = (S_0 - S_1)/(S_0 + S_1)$ , through  $C_{\text{opt}} = C/(2 - C)$  [23].
- [40] S. Schmitt, T. Gefen, F. M. Stürner, T. Uden, G. Wolff, C. Müller, J. Scheuer, B. Naydenov, M. Markham, S. Pezzagna, J. Meijer, I. Schwarz, M. Plenio, A. Retzker, L. P. McGuinness, and F. Jelezko, Submillihertz magnetic spectroscopy performed with a nanoscale quantum sensor, *Science* **356**, 832 (2017).
- [41] I. Lovchinsky, A. O. Sushkov, E. Urbach, N. P. de Leon, S. Choi, K. De Greve, R. Evans, R. Gertner, E. Bersin, C. Müller, L. McGuinness, F. Jelezko, R. L. Walsworth, H. Park, and M. D. Lukin, Nuclear magnetic resonance detection and spectroscopy of single proteins using quantum logic, *Science* **351**, 836 (2016).
- [42] N. Arunkumar, D. B. Bucher, M. J. Turner, P. TomHon, D. Glenn, S. Lehmkuhl, M. D. Lukin, H. Park, M. S. Rosen, T. Theis, and R. L. Walsworth, Micron-scale NV-NMR spectroscopy with signal amplification by reversible exchange, *PRX Quantum* **2**, 010305 (2021).
- [43] S. Sangtawesin, B. L. Dwyer, S. Srinivasan, J. J. Allred, L. V. H. Rodgers, K. De Greve, A. Stacey, N. Dontschuk, K. M. O'Donnell, D. Hu, D. A. Evans, C. Jaye, D. A. Fischer, M. L. Markham, D. J. Twitchen, H. Park, M. D. Lukin, and N. P. de Leon, Origins of Diamond Surface Noise Probed by Correlating Single-Spin Measurements with Surface Spectroscopy, *Phys. Rev. X* **9**, 031052 (2019).
- [44] X. Rong, J. Geng, F. Shi, Y. Liu, K. Xu, W. Ma, F. Kong, Z. Jiang, Y. Wu, and J. Du, Experimental fault-tolerant universal quantum gates with solid-state spins under ambient conditions, *Nat. Commun.* **6**, 8748 (2015).
- [45] T. Oeckinghaus, R. Stöhr, R. Kolesov, J. Tisler, F. Reinhard, and J. Wrachtrup, A compact, diode laser based excitation system for microscopy of NV centers, *Rev. Sci. Instrum.* **85**, 073101 (2014).
- [46] L. Robledo, L. Childress, H. Bernien, B. Hensen, P. F. A. Alkemade, and R. Hanson, High-fidelity projective read-out of a solid-state spin quantum register, *Nature (London)* **477**, 574 (2011).
- [47] R. Vasconcelos, S. Reisenbauer, C. Salter, G. Wachter, D. Wirtitsch, J. Schmiedmayer, P. Walther, and M. Trupke, Scalable spin-photon entanglement by time-to-polarization conversion, *npj Quantum Inf.* **6**, 9 (2020).
- [48] J. Storteboom, P. Dolan, S. Castelletto, X. Li, and M. Gu, Lifetime investigation of single nitrogen vacancy centres in nanodiamonds, *Opt. Express* **23**, 11327 (2015).
- [49] I. Meirzada, Y. Hovav, S. A. Wolf, and N. Bar-Gill, Negative charge enhancement of near-surface nitrogen vacancy centers by multicolor excitation, *Phys. Rev. B* **98**, 245411 (2018).
- [50] T. Gaebel, M. Domhan, C. Wittmann, I. Popa, F. Jelezko, J. Rabeau, A. Greentree, S. Prawer, E. Trajkov, P. R. Hemmer, and J. Wrachtrup, Photochromism in single nitrogen-vacancy defect in diamond, *Appl. Phys. B* **82**, 243 (2006).
- [51] P. Siyushev, H. Pinto, M. Vörös, A. Gali, F. Jelezko, and J. Wrachtrup, Optically Controlled Switching of the Charge State of a Single Nitrogen-Vacancy Center in Diamond at Cryogenic Temperatures, *Phys. Rev. Lett.* **110**, 167402 (2013).
- [52] J. C. Slater, The theory of complex spectra, *Phys. Rev.* **34**, 1293 (1929).
- [53] E. U. Condon, The theory of complex spectra, *Phys. Rev.* **36**, 1121 (1930).
- [54] R. Ulbricht and Z.-H. Loh, Excited-state lifetime of the NV<sup>-</sup> infrared transition in diamond, *Phys. Rev. B* **98**, 094309 (2018).
- [55] P. Deák, B. Aradi, T. Frauenheim, E. Jánzén, and A. Gali, Accurate defect levels obtained from the HSE06 range-separated hybrid functional, *Phys. Rev. B* **81**, 153203 (2010).
- [56] E. Londero, E. Bourgeois, M. Nesladek, and A. Gali, Identification of nickel-vacancy defects by combining experimental and *ab initio* simulated photocurrent spectra, *Phys. Rev. B* **97**, 241202(R) (2018).
- [57] Á. Gali, *Ab initio* theory of the nitrogen-vacancy center in diamond, *Nanophotonics* **8**, 1907 (2019).
- [58] Z.-H. Zhang, P. Stevenson, G. Thiering, B. C. Rose, D. Huang, A. M. Edmonds, M. L. Markham, S. A. Lyon, A. Gali, and N. P. de Leon, Optically Detected Magnetic Resonance in Neutral Silicon Vacancy Centers in Diamond via Bound Exciton States, *Phys. Rev. Lett.* **125**, 237402 (2020).
- [59] N. Mizuochi, T. Makino, H. Kato, D. Takeuchi, M. Ogura, H. Okushi, M. Nothaft, P. Neumann, A. Gali, F. Jelezko, J. Wrachtrup, and S. Yamasaki, Electrically driven single-photon source at room temperature in diamond, *Nat. Photonics* **6**, 299 (2012).
- [60] A. Lozovoi, H. Jayakumar, D. Daw, G. Vizkelethy, E. Bielejec, M. W. Doherty, J. Flick, and C. A. Meriles, Optical activation and detection of charge transport between individual colour centres in diamond, *Nat. Electron.* **4**, 717 (2021).
- [61] J. R. Maze, A. Gali, E. Togan, Y. Chu, A. Trifonov, E. Kaxiras, and M. D. Lukin, Properties of nitrogen-vacancy centers in diamond: the group theoretic approach, *New J. Phys.* **13**, 025025 (2011).
- [62] P. C. Maurer, G. Kucsko, C. Latta, L. Jiang, N. Y. Yao, S. D. Bennett, F. Pastawski, D. Hunger, N. Chisholm, M. Markham, D. J. Twitchen, J. I. Cirac, and M. D. Lukin, Room-temperature quantum bit memory exceeding one second, *Science* **336**, 1283 (2012).
- [63] J.-P. Tetienne, L. Rondin, P. Spinicelli, M. Chipaux, T. Debuisschert, J.-F. Roch, and V. Jacques, Magnetic-field-dependent photodynamics of single NV defects in diamond: an application to qualitative all-optical magnetic imaging, *New J. Phys.* **14**, 103033 (2012).
- [64] A. Gupta, L. Hacquebard, and L. Childress, Efficient signal processing for time-resolved fluorescence detection of nitrogen-vacancy spins in diamond, *J. Opt. Soc. Am. B* **33**, B28 (2016).
- [65] N. Kalb, P. C. Humphreys, J. J. Slim, and R. Hanson, Dephasing mechanisms of diamond-based nuclear-spin memories for quantum networks, *Phys. Rev. A* **97**, 062330 (2018).
- [66] G. Thiering and A. Gali, The  $(e_g \otimes e_u) \otimes E_g$  product Jahn-Teller effect in the neutral group-IV vacancy quantum bits in diamond, *npj Comput. Mater.* **5**, 18 (2019).